

# Design and Fabrication of a Customized Partial Hip Prosthesis Employing CT-Scan Data and Lattice Porous Structures

Jorge Corona-Castuera, Daniela Rodriguez-Delgado, John Henao, Juan Carlos Castro-Sandoval, and Carlos A. Poblano-Salas\*



Cite This: *ACS Omega* 2021, 6, 6902–6913



Read Online

ACCESS |

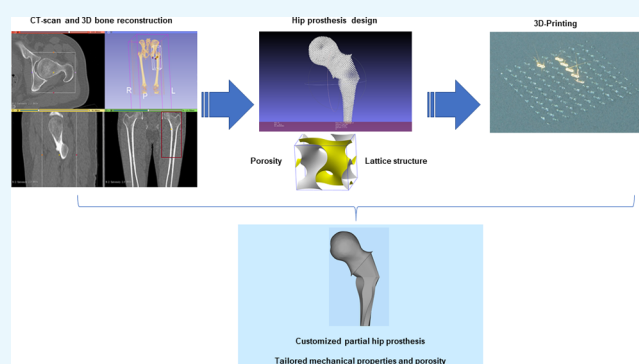


Metrics & More



Article Recommendations

**ABSTRACT:** As a larger elderly human population is expected worldwide in the next 30 years, the occurrence of aging-associated illnesses will also be increased. The use of prosthetic devices by this population is currently important and will be even more dramatic in the near future. Hence, the design of prosthetic devices able to reduce some of the problems associated with the use of current components, such as stress shielding, reduced mobility, infection, discomfort, etc., becomes relevant. The use of additive manufacturing (AM) and the design fabrication of self-supported cellular structures in the biomedical area have opened up important opportunities for controlling the physical and mechanical properties of hip implants, resulting in specific benefits for the patients. Different studies have reported the development of hip prosthetic designs employing AM, although there are still opportunities for improvement when it comes to customized design and tuning of the physical and mechanical properties of such implants. This work shows the design and manufacture by AM of a personalized stainless-steel partial hip implant using tomography data and self-supported triply periodic minimal surface (TPMS) cell structures; the design considers dimensional criteria established by international standards. By employing tomography data, the external dimensions of the implant were established and the bone density of a specific patient was calculated; the density and mechanical properties in compression of the implant were modulated by employing an internal gyroid-type cell structure. Using such a cell structure, the patient's bone density was emulated; also, the mechanical properties of the implant were fine-tuned in order to make them comparable to those reported for the bone tissue replaced by the prosthesis. The implant design and manufacturing methodology developed in this work considered the clinical condition of a specific patient and can be reproduced and adjusted for different types of bone tissue qualities for specific clinical requirements.



## 1. INTRODUCTION

Hip arthroplasty (HA) is a routinely performed medical procedure wherein a damaged hip is either totally or partially removed. Diseases such as tendinitis, fracture or dislocation, arthritis, osteoporosis, osteonecrosis, osteomyelitis, synovitis, and many others can lead to the need of a hip replacement.<sup>1</sup> Over the years, HA surgeries have been performed with generally successful outcomes using commercially available implants. These implants are manufactured in various countries and distributed and employed globally. According to Katz,<sup>2</sup> each manufacturer produces a variety of models with different predefined sizes and geometries to cover a wide range of patients and their specific needs. Consequently, it is common to find preferred implant brands and types in specific countries and among surgeons in the same geographical region. Nowadays, this situation is often observed in many countries as some clinicians have either become experts in a brand or

obtained successful outcomes using one or two specific types of implants in their communities.<sup>3,4</sup>

Although commercially available implants have had good acceptance in the medical community in the last 50 years, it is also true that post-HA surgery complications associated with predefined sizes and geometries of implants occur in patients all around the world.<sup>5–7</sup> According to Gwam et al.,<sup>8</sup> post-surgery complications can lead, in most of the cases, to a second revision surgery associated in some cases with infection, dislocation, and aseptic loosening, which evidently

**Received:** December 16, 2020

**Accepted:** February 23, 2021

**Published:** March 5, 2021



affects the patient's quality of life and increases hospitalization costs.

In the last decade, new manufacturing techniques have appeared in the market and attracted the attention of the biomedical industry due to the high potential they show to revolutionize implant technologies. 3D printing, also known as additive manufacturing (AM), has become more and more important in today's world due to its capacity to create objects from virtual 3D designs.<sup>9</sup> AM is based on the principle of layered manufacturing; specifically, some AM technologies such as direct metal laser sintering (DMLS) and electron beam melting (EBM) employ a high-power focus energy beam to melt metallic particles arranged in a powder bed and generating an object layer by layer.<sup>9,10</sup> With AM, the biomedical industry has a potential tool to manufacture implants with improved dimensional precision. AM can be employed to prepare personalized scaffolds and different kinds of implants based on patient's imaging data, such as CT or magnetic resonance.<sup>11,12</sup> In this way, the 3D printing technology brings real possibilities for building implant solutions tailored to specific patient needs.

DMLS and EBM have been used in recent years for the development of customized hip implants. In fact, previous studies developed by Cronskaer et al.<sup>13</sup> and Baharuddin et al.<sup>14</sup> have shown the feasibility of manufacturing Ti-6Al-4V femoral implants using DMLS and EBM. Customized implants for patients with a specific clinical condition and anatomy are currently a major need to minimize the risk and complications associated with the use of current predefined commercial hip implants.

Customized implants are becoming a better option than conventional counterparts as the former can be manufactured according to the size and structure of the patient's anatomy, resulting in highly accurate implant fitting. For instance, in a previous study performed by Abdul and Kamsah,<sup>15</sup> it has been suggested that for hip implants, by maximizing the stem-bone contact, a reduction of micromovements, and therefore improved fixation stability, can be achieved. The authors reported that by performing a correct fitting and filling of the medullary cavity with the implant, a better distribution of mechanical stresses toward the proximal part of the femur can be assured, hence preventing axial and torsional instabilities associated with aseptic loosening and failures observed in commercial implants.<sup>16,17</sup> Another advantage of customization is that implants can be manufactured having similar density and stiffness to those of the patient's bone. Fully dense commercial hip prostheses are commonly fabricated from Ti-based or CoCr-based alloys showing a stiffness up to 9 times higher than that of the human bone they replace. Then, when a conventional fully dense hip implant replaces the patient's bone, loading conditions change and promote that most of the mechanical load is transferred to the implant. In fact, it has been reported that in healthy individuals, about 3.3 times the weight of a person is supported by the pelvis and femur and transmitted through the hip joint head during day-to-day activities.<sup>18</sup> Hence, when high density-stiffness implants are employed, the bone around the implant is subjected to low mechanical load levels; such a phenomenon is known in orthopedy as stress shielding and is another cause of commercial implant failure and removal. A thorough review of stress shielding can be found in research studies reported by Sundfeldt et al.<sup>16</sup> and Piao et al.<sup>19</sup> Previous studies have proposed the fabrication of porous implants by additive

manufacturing as a solution for stress shielding.<sup>20–22</sup> The main characteristic of this type of implants is the introduction of porous lattice structures to obtain a similar elastic modulus and density to those of the human bone.

Lattice structures are topologically ordered three-dimensional open-celled structures composed of one or more repeating unit cells and have shown to be a good option for the development of porous implants. Previous studies have reported the development of lattice structures based on triply periodic minimal surfaces (TPMSs) by additive manufacturing. For instance, Hussein et al.<sup>23</sup> fabricated diamond and gyroid structures based on TPMS from 316L stainless-steel, Ti-6Al-4V, and AlSi10Mg powders by DMLS. The authors reported that these types of structures presented an elastic modulus and an elastic limit that increased with an increase in relative density. Interestingly, they also reported that lattice structures obtained from Ti-6Al-4V powders showed 3 to 4 times higher elastic modulus than those manufactured from 316L stainless-steel and AlSi10Mg powders, having the same relative density and unit cell size. Yan et al.<sup>24</sup> have also developed gyroid and diamond structures from Ti-6Al-4V powders by DMLS. They reported relative porosity values between 80 and 95% and pore size values from 480 to 1600  $\mu\text{m}$ . These structures presented a mechanical response that was dependent on their relative density; this allowed the design of lattice structures with similar mechanical properties to those of bone. In this manner, the authors reported lattice structures with elastic modulus values from 0.12 to 1.25 GPa, which were close to those reported for trabecular bone. Maietta et al.<sup>25</sup> designed and produced lattice structures by selective laser melting (SLM) employing a Ti-6Al-4V alloy; by performing experimental and theoretical analyses, the authors demonstrated that it is possible to modify the geometry and pore size of the structures without altering their mechanical performance. Such modifications can be quite attractive for biomedical applications in which mass transport properties may be required. Simoneau et al.<sup>26</sup> demonstrated the feasibility of producing a commercial stem by DMLS with an internal porous structure. Other studies have demonstrated, by designing a hip implant employing finite element analysis, that the use of porous structures can significantly reduce stress shielding.<sup>21,27</sup> Overall, in different studies, it has been shown by numerical simulation that lattice structures can be attractive for the fabrication of implants by additive manufacturing.<sup>28,29</sup>

The present study proposes the design and manufacturing of a partial hip prosthesis based on: (i) CT-scan data from the anatomy of a real patient, (ii) design guidelines included in ISO standards, and (iii) experimental validation employing two different types of lattice structures. It is important to remark that a key process in hip replacement surgery is preoperative planning. Such planification is the first step to follow when an HA surgery is performed and must be carried out very carefully to avoid postoperative problems. This first step includes disease identification, anatomy studies, determination of implant sizing and positioning, and evaluation of risks during surgery. For the case of customized implants including internal self-supported structures, the inclusion of a porous structure design/selection step in the preoperative plan is fundamental. Abbaszadeh et al.<sup>30</sup> have developed a methodology for designing customized hip implants based on bone CT-scan images and considering intramedullary and extramedullary bone portions as part of the design criteria. The intramedullary part of the implant was designed based on an accurate and detailed description of the 3D geometry of the femoral

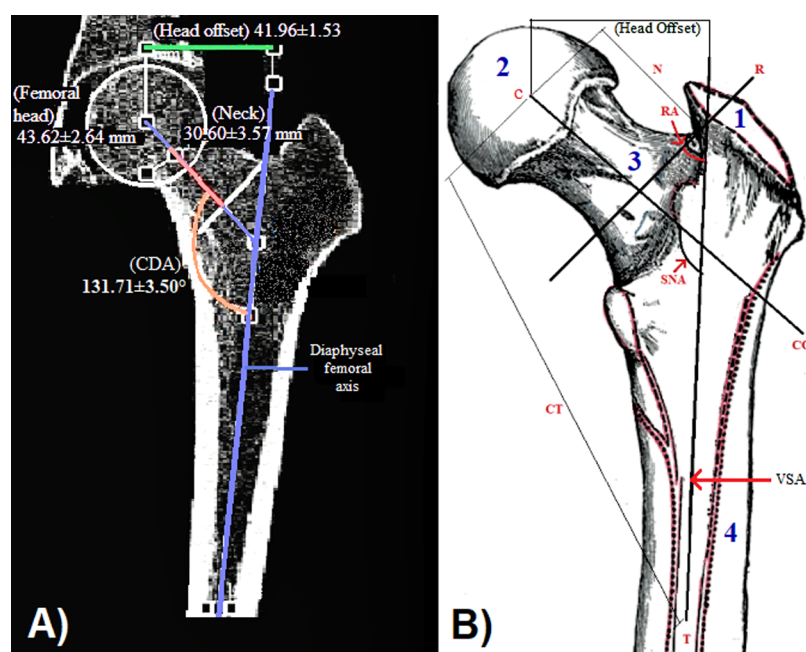


**Figure 1.** (a) CT-scan image obtained from the patient's affected area including relevant actual bone dimensions. (b) Schematic representation of the bone displaying the characteristic lengths and angles (highlighted in red) defined by the ISO 7206-1 standard.<sup>32</sup> Numbers in bold indicate the four different regions in which the bone's apparent density was evaluated.

intramedullary cavity in order to improve the fit-and-fill performance of the femoral stem. Recently, Mangano et al.<sup>31</sup> reported a similar methodology based on CT-scan images for the fabrication of custom-made DMLS-printed subperiosteal implants, in particular for the restoration of an atrophic posterior mandible in an elderly patient. Thus, implant design, employing CT-scan data, as part of preoperative planning seems to be a frequently accepted procedure for surgical interventions involving implant customization.

In the literature, it is fairly common to find research studies dealing with the design of implants by conventional methods and also by additive manufacturing, based on commercial geometries but without considering guidelines suggested by international standards. The present study shows the development of a methodology for hip implant design from CT-scan data; it also includes a methodology for obtaining anatomical features from a selected patient potentially suitable for HA surgery. Also, the study validates a model for a partial hip prosthesis by following recommendations from international standards. Finally, by employing the proposed methodology, an optimized partial hip prosthesis was designed and 3D-printed by DMLS including internal cellular structures for providing desired physical and mechanical properties.

## 2. RESULTS AND DISCUSSION

**2.1. Anthropometric Study.** Figure 1a shows a CT-scan image obtained from the patient's hip. Different measurements were performed to the patient's femoral area, specifically by analyzing the coronal anatomical plane. The following average values were obtained from a set of tomography images: a femoral head diameter of  $43.62 \pm 2.64$  mm, a femoral head offset of  $41.96 \pm 1.53$  mm, and a cervical-diaphyseal angle (CDA) of  $131.71 \pm 3.50^\circ$ . These measurements are important when proposing any implant design. In fact, guidelines included in the ISO 7206-1 standard<sup>32</sup> indicate three key values for establishing a hip implant design: (i) the virtual stem

axis (VSA), (ii) the angle formed by the longitudinal axis of the femoral neck and the longitudinal axis running from the center of the femoral stem to meet the neck axis (SNA), and (iii) the distance between the center of the femoral head and the center of the VSA axis (CT distance); these dimensions are indicated in Figure 1b. The standard also suggests a  $135^\circ$  value for the SNA angle and a minimum CT distance of 120 mm. These values are established to ensure fixation of the prosthesis and restoration of joint mobility when commercial prostheses are used since, statistically, the referred values are representative of a very well-documented population.

In the present study, the design of the partial hip prosthesis started by matching the virtual stem axis (VSA) with the patient's diaphyseal femoral axis (outlined in blue in Figure 1a). Also, a CT distance recommended for a short stem prosthesis was considered.

The CDA and SNA angles were assumed to be identical (both depicted in Figure 1a,b, respectively). CDA angle values ranged between  $128.21$  and  $135.21^\circ$ , and the variation in CDA values obtained from CT-scan images is attributed to data quality, which may include noise or artifacts and also to human errors or imprecisions while performing the measurements employing image analysis software. The CDA range is comparable with the angle value suggested by the ISO 7206-1 standard ( $135^\circ$ ).<sup>32</sup> Therefore, by considering the CT-scan measurements and recommendations included in such a standard, a CDA angle of  $135^\circ$  was employed as a reference for designing the hip prosthesis in the present study.

The density of both cortical and trabecular bone tissue located at different regions in the femur was calculated. Density calculations were performed slice-by-slice within a selected ROI until a complete volume was covered. An average value of the calculated apparent density from different regions of the patient's bone is reported in Table 1; specifically, the proximal femur was divided into four regions to evaluate the apparent density of bone. Figure 1b shows such regions as



**Table 1. Apparent Density of Trabecular and Cortical Bone Calculated from CT-Scan Image Analysis**

region of proximal femur	apparent density (g/cm <sup>3</sup> )
femoral head	0.72 ± 0.69
neck	0.46 ± 0.08
greater trochanter	0.20 ± 0.27
diaphysis	1.55 ± 0.20

follows: (1) greater trochanter, (2) femoral head, (3) neck, and (4) diaphysis. Apparent density of trabecular tissue was calculated from regions 1 to 3, whereas region 4 served as a reference for calculating the same property for cortical bone.

Density values included in Table 1 agree with those reported previously in the literature; for instance, typical apparent density values reported for trabecular bone are in the range from 0.4 to 1.1 g/cm<sup>3</sup>.<sup>33</sup> This range of values showed that for this particular case, important variations in density of trabecular bone tissue were found in the femoral area. One can observe that the calculated density value at the femoral head is higher than that of the neck and trochanter, respectively. As expected, a higher apparent density was found in the diaphysis as large areas of cortical tissue were found in that region. The apparent density calculated for cortical bone tissue at the diaphysis fell within reported values, that is, 1.26–2.34 g/cm<sup>3</sup>.<sup>33</sup> It is important to point out that the medical interpretation of the CT-scan data presented in Section 2 suggested degenerative osteoarthropathy in the patient, which is one of the common musculoskeletal diseases seen in elderly people. In order to further investigate the medical condition of the patient and, in particular, to reveal his femoral bone quality state, a T-score parameter from Hounsfield (HU) units was calculated. The T-score parameter is established by the World Health Organization (WHO) as an efficient way to evaluate the bone quality of a patient with respect to a healthy individual. Hendrickson et al.<sup>34</sup> calculated this parameter as the difference between the patient bone mineral density (BMD) and the BMD mean value reported for a reference population divided by the standard deviation from BMD data of such population, as can be seen in the following equation

$$T\text{-score} = (HU - \mu_{\text{ref}}) / \sigma_{\text{ref}} \quad (1)$$

By applying equation 1, a T-score for the patient studied in this work was calculated. The patient BMD was obtained from an average of the HU values measured on the patient's femoral head region employing CT-scan data. The reference BMD values were also obtained from HU measurements performed on CT-scan data taken from a healthy and young individual. Hence, a T-score of −2.36 was calculated for our patient. Such a result confirms the patient's clinical diagnosis made from the CT-scan study corresponding to degenerative osteoarthropathy. According to the World Health Organization, T-score values between −1.0 and −2.5 are related to reduced bone density (osteopenia), whereas values ≤ −2.5 correspond to osteoporosis.<sup>34</sup>

The main purpose of calculating apparent density values for both trabecular and cortical tissue was to use those values to produce porous structures and gyroid-type lattices, having similar density levels to those found in each region of the proximal femur. By having a hip prosthesis with density levels similar to the original tissue, a similar mechanical response to that of the bone to be replaced would be expected, leading to a

desired mechanical stress distribution and reducing the occurrence of stress shielding.

**2.2. CAD Design of a Customized Partial Hip Prosthesis.** After studying the patient's medical condition, data obtained from both the anthropometric study based on CT tomography and from the ISO 7206-1 standard<sup>32</sup> were considered for the final design of the partial hip prosthesis. This information defined the overall dimensions and the external geometry of the implant. The design of the partial hip prosthesis starts by a careful selection of angles and dimensions according to the patient's anatomy, that is, cervical-diaphyseal angle, CT length, femoral head offset, and resection angle. Specifically, to design a prosthesis with an SNA angle of 135°, a line was drawn from the center of the femoral head through the center of the femoral neck, dividing the femoral neck into two identical parts; in addition, a vertical line emulating the virtual stem axis was also drawn, ensuring an SNA angle of 135° at the intersection with the first line. Once the SNA angle was defined, a CT distance of 120 mm was included in the design by drawing a line from the bottom center of the stem to the center of the femoral head. Figure 2 shows the relevant dimensions employed in the hip implant design proposed in this work.

Another important characteristic of a hip prosthesis is its volume shape. In the present study, the volume shape of the partial hip prosthesis was designed according to the shape of the medullary cavity, that is, taking advantage of medical images for customization. In order to replicate the shape of the femoral medullary cavity, that is, the cavity where the prosthesis is inserted, an axial cut-by-cut reconstruction of the cavity was performed, that is, along the entire femur length. By following this procedure, a complete reconstruction of the medullary cavity was obtained; the cavity's volume shape was then employed for designing the partial hip stem in order to guarantee an optimized fitting with the patient's femoral cavity.

It is important to remark that not only anatomical distances, angles, and volume shapes are crucial for prosthesis performance but also the surface shape may also have an important influence on the biomechanical response of cement-less implants. For instance, curved smooth surfaces are usually associated with a reduction of stress concentration at the implant surface, which can increase its fatigue life. Alternatively, stems with stepped surfaces and some having vertices are often included in cementless implants to provide good anchoring capability, preventing sliding at the bone/implant interface. However, this option is often related to high stress concentrations, which can affect fatigue life. Two different surface shape options were included in the customized design in the present study, the first having an external heptagonal geometry conceived to establish contact points with the medullary canal and avoiding rotation of the prosthesis. The second stem was designed with the geometry of the medullary cavity, trying to fit and fill the whole cavity to obtain improved mechanical stability and a better stress distribution. Figure 2a,b shows both designs including a transversal view of the stems. Surface shape geometry was included in the present study only as a design task that must be considered in any customized implant design; however, it is important to point out that the mechanical performance validation of the designed parts is quite relevant and is out of the scope of the present research. Both designs will be evaluated in a future study by FEA in order to establish their contribution to stress shielding, fatigue

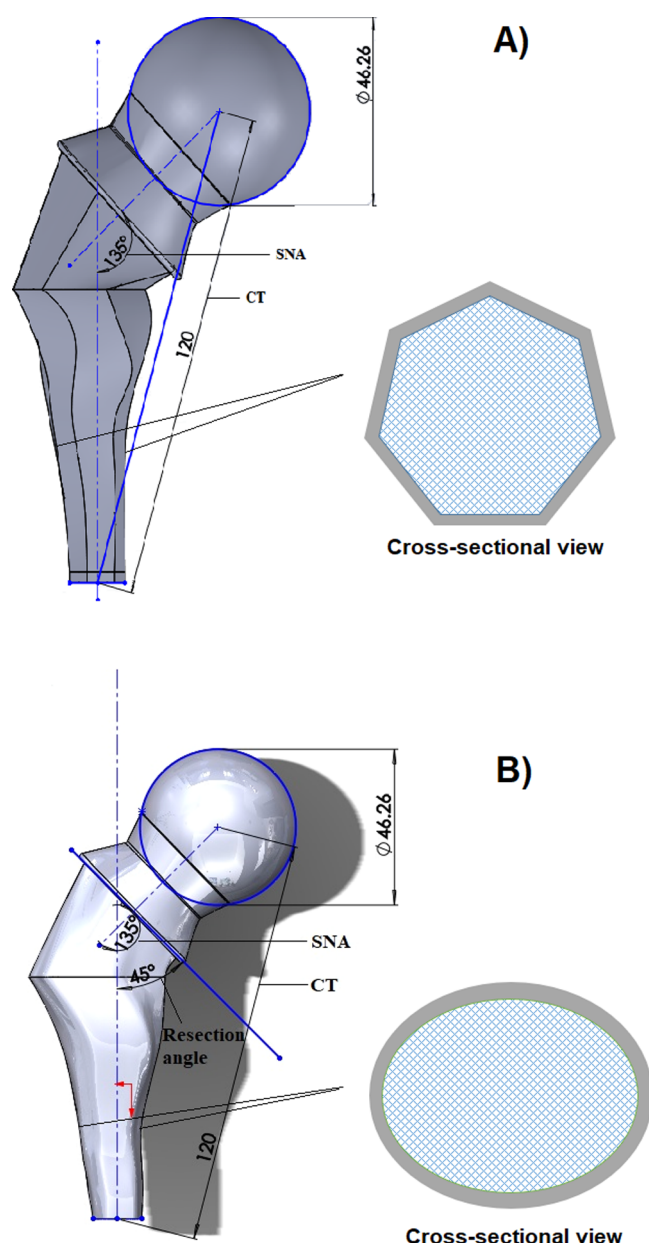


**Figure 2.** Partial hip prosthesis designs proposed in this work: (a) heptagonal cross-sectional stem and (b) smooth cross-sectional stem.

resistance, mechanical anchorage, and bone-implant micro-movements when included in the prosthetic design.

In order to complete the partial hip stem design, the resection angle and femoral head diameter were also carefully selected according to the patient's anatomical data. The resection angle is associated with the orientation of the surgical cut plane; in this study, a 45° resection angle was established according to a previous study by Muñoz Gutierrez.<sup>35</sup> On the other hand, as previously observed in Figure 1, the femoral head of the patient's bone had an irregular shape, which is a normal configuration of human joints. Nevertheless, this irregular shape is not mechanically recommended for artificial joints since aggressive wear can occur, promoting implant failure. Therefore, the femoral head design, in the present study, was approximated to a sphere with a smooth surface, which is the current trend in orthopedics for this kind of component. It is important to point out that the femoral head

diameter was adjusted to make a conversion from the irregular shape observed from medical images to the spherical design. Such a design considered an average dimension taken from front, right, and top planes from the patient's femoral head.

On the other hand, the results obtained from the study of self-supported structures yielded relevant design information for the inner part of the prosthesis to meet the desired requirements of density and mechanical resistance, that is, a density comparable to that of the bone tissue calculated from CT-scan data and an elastic modulus and compressive strength within values reported for femoral cancellous bone tissue from patients with osteoarthritis.<sup>36</sup> A description of the physical and mechanical properties obtained in the cellular structures designed and fabricated in this work is included in the following sections.

**2.3. Porous Lattice Structures.** **2.3.1. Density Versus Geometry Variations.** Density measurements of three samples per lattice structure were performed; in particular, the variation of density as a function of  $t$  parameter for both simple and double gyroid structures was studied. The  $t$  parameter in gyroid-type structures is mainly related to the wall thickness and, therefore, has an important influence on the mechanical response of such structures. Equations 2 and 3, obtained from the experimental results, describe the behavior of density as a function of  $t$  parameter for both simple and double gyroid structures. Both expressions are valid for samples fabricated employing 17-4 PH stainless steel.

$$\frac{\rho_{\text{sample}}}{\rho_{\text{material}}} = 0.5684t + 0.0082 \quad (2)$$

$$\frac{\rho_{\text{sample}}}{\rho_{\text{material}}} = -0.3343t + 0.4519 \quad (3)$$

Figure 3 shows the variation of apparent density as a function of  $t$  parameter for 17-4 PH stainless-steel simple and

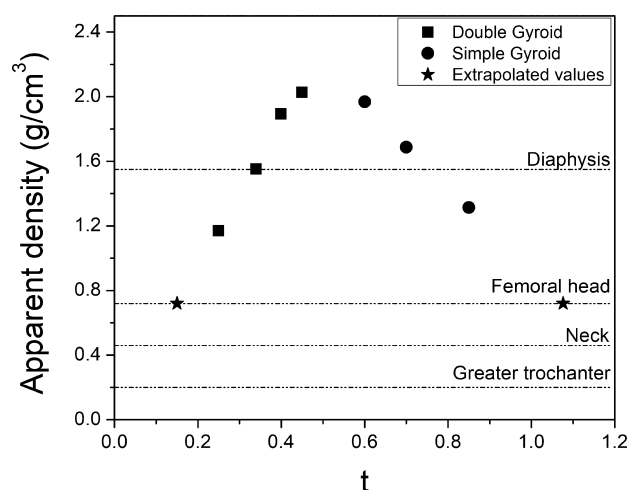


**Figure 3.** Apparent density of simple and double gyroid structures as a function of  $t$  parameter. The dashed lines display the density levels for different femoral regions calculated in this work.

double gyroid structures. As can be seen from Figure 3, some structures showed apparent density values between the density levels calculated in this work for the femoral head and the diaphysis. Interestingly, the double gyroid structure with a 0.3  $t$  value showed a comparable density to that calculated for the

diaphysis. Also, for both structures, increased density values were observed as the  $t$  parameter was close to 0.5, such structures showed higher density values than those calculated for the diaphyseal region. As the main region to be replaced by the prosthesis is the femoral head, a lattice structure having a density close to that region is desired for designing the implant. By using both gyroid structures, the femoral head density would be attained, that is, with a  $t$  parameter of 0.150 and 1.076 for the double and simple gyroid structures, respectively (extrapolated values employing eqs 2 and 3 are depicted as stars in Figure 3).

**2.3.2. Compression Test.** For uniaxial compression tests, simple and double gyroid-type cubic samples of  $10 \times 10 \times 10$  unit cells (with three specimens for each condition) were manufactured according to the ISO 13314 standard.<sup>37</sup> Figure 4

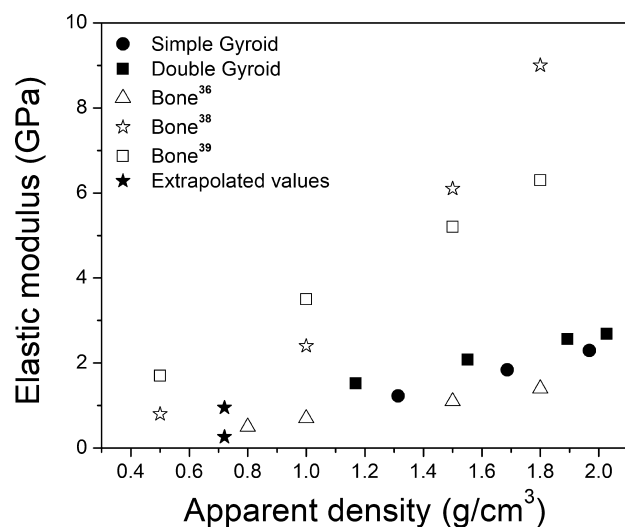


**Figure 4.** Results of  $E$  obtained from compression tests vs apparent density.  $E$  data from previous studies of trabecular femoral bone tissue are included.<sup>36,38,39</sup>

shows the variation of elastic modulus in compression as a function of apparent density for both structures, data reported in the literature are also included as a reference. The results obtained in this research follow a similar trend to that reported in a work by Li and Aspden,<sup>36</sup> in which the authors studied the mechanical properties of cancellous bone from the femoral region of patients suffering from osteoporosis. It is then demonstrated that the stainless-steel TPMS structures developed in this work show physical and mechanical properties comparable to those reported for femoral human bone tissue.

As mentioned before, the target density value for the prosthesis design is a value close to that of the patient's femoral head, that is,  $0.72 \text{ g/cm}^3$  (stars in Figure 3). Such a density value is also indicated in Figure 4 as solid stars in order to show the corresponding elastic modulus value for the TPMS structures. Elastic modulus values of 0.25 and 0.95 GPa were obtained for the simple and double gyroid structures respectively, falling within the trend reported in previous studies for femoral human bone.<sup>36,38,39</sup> These elastic modulus values would be expected in the final prosthesis if TPMS structures employed are designed to replicate the patient's femoral bone density.

The range of maximum compression stress values for both cortical and trabecular bone tissue reported in the literature are

presented in Figure 5 as striped areas.<sup>40–42</sup> Figure 5 also shows the results of maximum compression stress (solid squares and

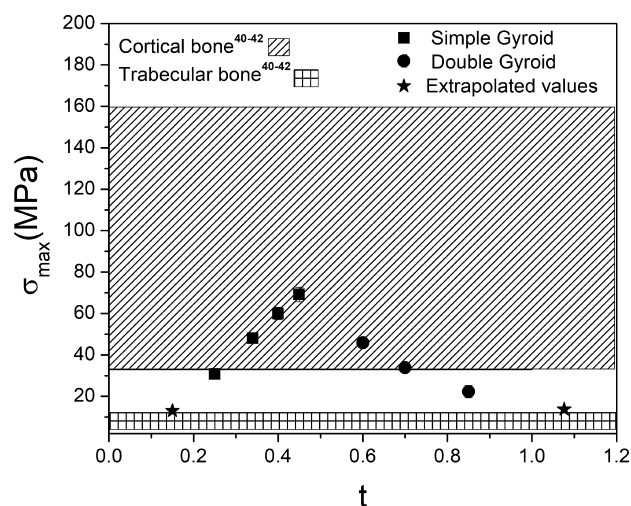


**Figure 5.** Results of maximum compression stress vs  $t$  parameter.

circles) obtained experimentally for the gyroid-type structures in the present study; most of the measured compressive strength values are in the range reported for cortical bone, whereas few of them laid outside this range ( $<30 \text{ MPa}$ ). The solid stars depicted in Figure 5 show extrapolated values of maximum compression stress corresponding to the compressive stress reported for trabecular bone. For the gyroid structures with the same value of femoral density ( $t$  parameter of 0.150 and 1.076), extrapolated compressive strength values obtained are comparable to those of trabecular bone ( $14 \text{ MPa}$ ).

In order to reveal the effect of cell size on the maximum compression stress achievable on the TPMS structures, further experiments were carried out on new samples selecting a specific and constant  $t$  parameter for each type of structure ( $t = 0.34$  and  $t = 0.76$  for double and simple gyroid, respectively) and varying the cell size. Figure 6 shows the results of maximum compressive stress as a function of cell size. For the simple gyroid structure, the maximum compressive stress

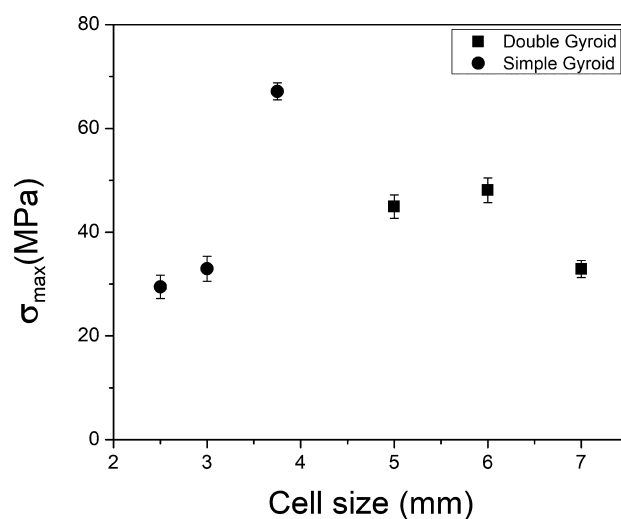


**Figure 6.** Results of maximum compression stress vs cell size ( $t = 0.34$  and  $t = 0.76$  for double and simple gyroid, respectively).



values increased as the cell size was close to 4 mm, while the compressive stress value for the double gyroid structure reached its maximum around a 6 mm cell size. It is important to point out that cell size is a parameter that does not affect the apparent density of the structure. Then, this result shows that cell size can be a useful parameter for tuning compressive properties if required to approach the mechanical properties of the structure, while keeping its density constant. In the present study, a cell size of 3 mm was selected for the fabrication of the TPMS structures since, as observed in Figures 4 and 5, mechanical properties of structures are similar to those of bone tissue.

Based on experimental results, the simple gyroid structure with a 1.076  $t$  value was selected over the double gyroid structure with a 0.150  $t$  value for the fabrication of the inner part of the hip implant. The selected TPMS structure in this work showed density and elastic modulus comparable to the values reported for the bone tissue that will be replaced by the proposed hip prosthetic device. Therefore, by employing 17-4 PH stainless steel for the fabrication of such structures, it was possible to reproduce the physical and mechanical properties of bone tissue found in femoral components.

Figure 7 shows the customized hip prosthesis manufactured by DMLS employing 17-4 PH stainless steel. The prosthesis

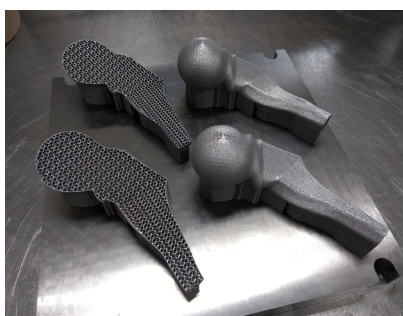


Figure 7. DMLS-printed customized hip prosthesis.

was printed in two-halves in order to visually show its inner structure, which is composed of a gyroid structure, emulating the femoral density of the patient studied in the present work. Interestingly, for the selected patient, the prosthesis was customized according to his average femoral bone density

(0.72 g/cm<sup>3</sup>), corresponding to a customized prosthesis with a total weight of 72.44 g. This weight value is almost 10 times lower than that expected for a fully dense prosthesis having the same dimensions and fabricated employing the same material (751.14 g). In this manner, this customized prosthetic device would likely offer a better sense of comfort to the patient than a conventional solid counterpart.

### 3. CONCLUSIONS

The present study provides a systematic methodology for the design and customization of a partial hip prosthesis based on medical images of a potential candidate for a hip surgery. CT-scan was performed on the patient's hip and the resulting images were analyzed using commercial software in order to evaluate the bone's density distribution in the affected zone. The reconstruction of the bone was the basis for proposing an implant design that follows the anatomy of the selected patient, while keeping established dimensions suggested by international standards for the fabrication of hip implants. The introduction of a complex porous structure in the design of the prosthesis is a key factor to emulate the osseous structure of the patient. The use of TPMS structures is a good alternative to approach the density and mechanical properties of the implant to those of the bone to be replaced. Specifically,  $t$  parameters in TPMS structures can be employed to adjust the density of the structure to the density value required for the patient, while cell size can be adjusted to approach the mechanical properties of the structure to the expected value in the bone. The selection of density and mechanical strength of the prosthetic device should be performed according to the patient's medical condition and also by considering the expertise of specialized clinicians. As the methodology employed in the present study considers the clinical condition of the patient, it can be reproduced and tuned for different bone quality conditions and specific density-strength requirements.

### 4. MATERIALS AND METHODS

#### 4.1. Customized Hip Prosthesis Design Methodology.

Figure 8 summarizes the methodology employed in the present study to develop a customized partial hip implant for a selected patient. Step 1 involves acquisition of anatomical data and selection of a patient (see details in Sections 4.2 and 4.3). Data

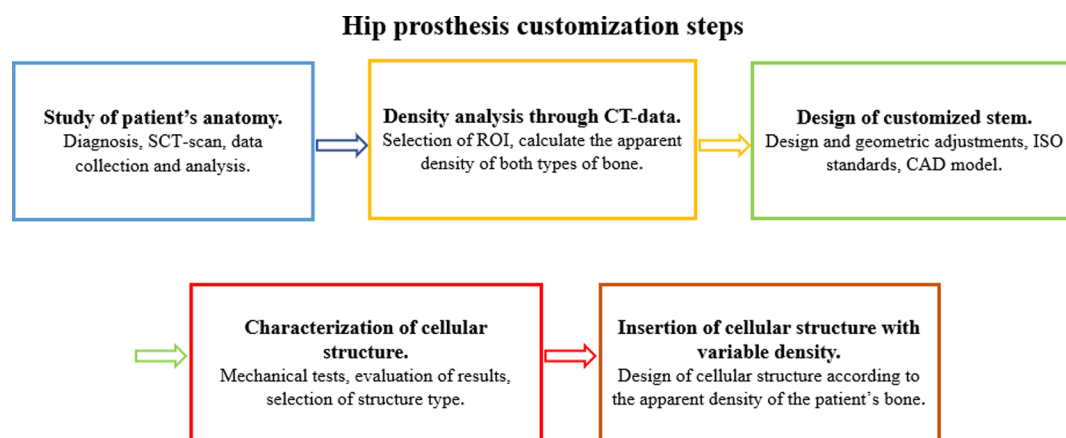
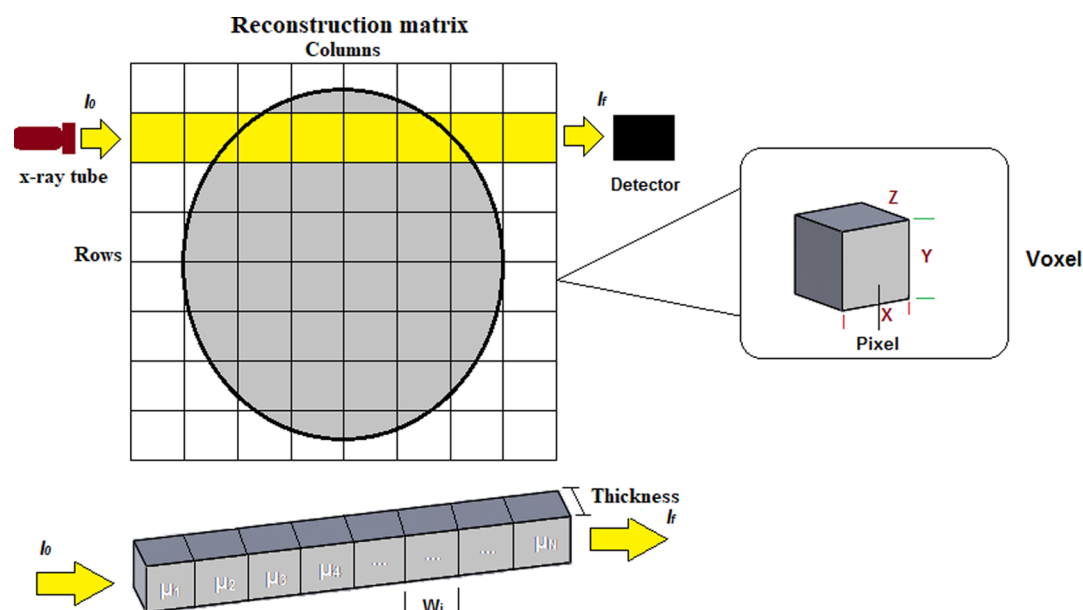


Figure 8. Methodology for design and fabrication of customized prosthesis: (1) study of patient's anatomy, (2) density analysis from CT-scan data, (3) design of customized prosthesis, (4) characterization of cellular structure, and (5) insertion of the cellular structure with variable density.



**Figure 9.** Schematic representation of a CT image and voxels;  $\mu_1$  to  $\mu_N$  represent different attenuation coefficients.

obtained in step 1 are then used to build up a model of the patient's bone including relevant features such as density and medullary cavity volume (see details in Section 4.4.1). Once the patient's bone CAD model is obtained, a CAD model of the hip prosthesis is then designed (see details in Section 4.5). Afterward, porous lattice structures are designed to emulate the porosity of the patient's bone and a set of experiments are carried out to evaluate the correlation between mechanical properties and density, in order to satisfy the patient's medical requirements (see details in Section 4.6). Finally, the improved prosthesis CAD design is processed and printed by additive manufacturing (DMLS) to obtain the final personalized component (see details in Section 4.7).

**4.2. Computerized Tomography (CT Scan).** Non-invasive data acquisition from the patient's anatomy was conducted by CT scan. Data acquisition was focused on a region of interest (ROI) that included the pelvic and femoral area of a selected patient. CT scan was performed employing a Biograph 64 PET/CT Truepoint tomograph (Siemens AG), operating at 120 kV and 200 mA. The obtained images had a  $512 \times 512$  pixel resolution. CT-scan data were obtained from a series of transversal slices with a 0.6 mm thickness along the ROI. A total of 1047 images were acquired and exported into a digital imaging and communications in medicine (DICOM) format for further processing.

**4.3. Patient Selection.** A 60 year-old male was selected for performing a CT-scan study in order to obtain information for the calculation of femoral bone density. The patient reported not having any relevant pathology. A written consent was signed by the patient before the CT-scan study was carried out; also, an IRB approval was obtained in order to perform this research. Single-phase CT scan of thigh axial cuts, coxofemoral joints, and knees was performed. Multiplanar reconstructions were carried out by following a procedure developed along with the CT-scanner supplier. The main reported findings from the CT-scan study were (i) muscular planes with reduced volume substituted by fat tissue, (ii) minor calcification (<5 mm) of subcutaneous cellular tissue at the left patellar region, (iii) the studied bone structures showed degenerative changes characterized by marginal osteophytes

and widespread bone density; (iv) minimal sclerosis was observed in coxofemoral, femoropatellar, and femorotibial joints, and irregular borders were observed in all joints; (v) subchondral cyst was found in femoropatellar joints, and (vi) there were no data suggesting the presence of intra-articular edema or injury. The clinical diagnosis indicated the presence of anatomical evidence compatible with degenerative osteoarthritis.

**4.4. Bone and Medullary Cavity Reconstruction.** 3D Slicer software was employed to process the collected tomographic data in order to reconstruct the patient's bone. Initially, each CT-scan image in DICOM format, from the ROI, was loaded into the software and treated to extract bone tissue information. Bone data from the proximal femoral region were delimited and a grayscale threshold was selected to differentiate data from bone and muscle; then, Hounsfield units (HU) were employed to obtain information from both trabecular and cortical bone tissue. A segmentation mask with a threshold value between 230 and 2321 HU was employed to perform a 3D reconstruction of the femur. In addition, a segmentation mask with a threshold value between -360 and 680 was used for the 3D reconstruction of the femoral cavity. By following this thresholding procedure, an interpolation of the CT images was performed to delimit the bone/internal tissue interface in order to obtain the internal geometry of the medullary cavity. The reconstructed patient's bone and medullary cavity volume were finally converted into a CAD file, which then was employed as a reference for the design of the customized implant stem.

**4.4.1. Bone Porosity Distribution.** Calculation of bone density was carried out by analyzing the patient's CT-scan data from the ROI. It is well-known from radiology that grayscale units, obtained from tomography, can be transformed into radiographic density data. Figure 9 represents a CT image which is known as a reconstruction matrix, in this case, the cross-sectional image of a patient's scanned body part. This image consists of columns and rows that define 2D elements known as pixels (represented in the image as squares). Each pixel represents a brightness level which, in turn, depends on the interaction between X-rays and the tissue distribution



within the patient's scanned body part. In a digital CT image, a pixel is always associated with a voxel. Voxels are an array of elements of volume that constitute a notional three-dimensional space; that is, they are a 3D representation analogue of a pixel and relate both pixel size ( $X$  and  $Y$  plane in Figure 9) and slice thickness ( $Z$  direction in Figure 9). The CT-scan image obtained from the patient's body, irradiated with X-rays, is a reconstruction from a large number of measurements of attenuation coefficients, which are a measure of how easy bone and/or tissue can be penetrated by X-rays. A CT-scan detector measures an X-ray signal that is proportional to the sum of the attenuation coefficients of the studied body segment. Therefore, a CT-scan image contains information about volumetric characteristics of bone and can be employed to obtain data from bone tissue volumetric porosity; such calculation is a fundamental part of the present study as it proved to be quite useful for the design of a specific-patient's customized stem with specific physical and mechanical properties, which may be useful for minimizing stress shielding in patients subjected to HA surgery.

Radiographic density is then a measurement of the degree of X-ray attenuation in the body segment studied and can be used for the calculation of bone tissue volumetric density. According to previous studies, radiographic density from CT-scan images can be determined by employing the following equation<sup>43,44</sup>

$$\rho_{\text{qct}} = 0.0007764(\text{HU}) - 0.0056148 \quad (4)$$

where HU are Hounsfield units, also obtained from patient's CT-scan images. In previous research studies, the use of bone ash density to correlate radiographic data with bone volumetric density values has been proposed.<sup>43–49</sup> Ash density is defined as the bone density measured after the bone is incinerated under controlled conditions. In this manner, trabecular and cortical bone show a particular ash density value that can be correlated with radiographic data for each type of tissue. Radiographic density of trabecular (TB) and cortical bone (CB) can be calculated according to the following equations

$$\rho_{\text{qct}} = 0.98\rho_{\text{ash}} - 0.05 \quad (5)$$

$$\rho_{\text{qct}} = 1.07\rho_{\text{ash}} + 0.01 \quad (6)$$

In the present study, ash densities of trabecular and cortical bone from the selected patient were calculated from CT images and employing eqs 4–6. In order to transform ash density obtained from radiographic data to volumetric density values, the following equations have been proposed.<sup>44,49</sup>

$$\rho_{\text{app}} = 3.69\rho_{\text{ash}} - 0.26 \quad (7)$$

$$\rho_{\text{app}} = 1.58\rho_{\text{ash}} + 0.11 \quad (8)$$

Equations 7 and 8 were employed in this research to calculate the volumetric density of both trabecular and cortical bone.

**4.5. CAD Design of a Customized Partial Hip Prosthesis.** A partial hip prosthesis was designed by following the guidelines included in the ISO 7206-1 standard,<sup>32</sup> in which specific guidelines for establishing the dimensions of partial and total hip joint prostheses are included; the design was also based on an anthropometric analysis of the patient's femoral region. The final dimensions of a partial hip joint prosthesis have a significant influence on the successful recovery of mobility in a patient. Of particular interest are the guidelines

regarding specific angles and dimensions in the prosthesis required to maintain anatomic harmony. Anatomical measurements from the patient's femur were carried out on CT-scan images following the recommendations included in the aforementioned standard. Both femoral head and stem were designed by employing SolidWorks software based on a 3D reconstruction of the patient's femur and medullary cavity.

**4.6. Design and Experimental Validation of Porous Lattice Structures.** A couple of TPMS lattice structures were selected in the present study to be included in the final partial hip prosthesis design in order to control its physical and mechanical properties. In particular, two lattice structures based on Schoen's gyroid surface, namely, simple gyroid and double gyroid, were designed employing MATLAB and MeshLab software, as shown in Figure 10.

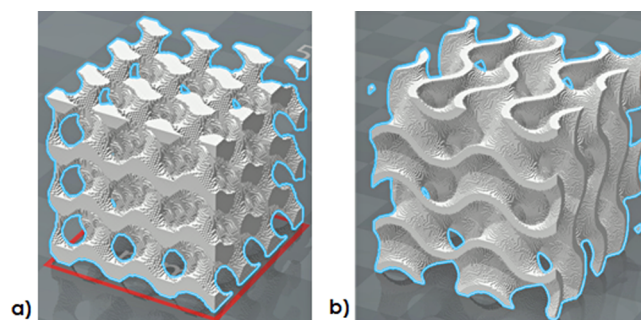


**Figure 10.** Lattice structures designed using MATLAB and MeshLab: (a) simple gyroid and (b) double gyroid.

The theoretical mathematical formulations for the development of simple and double gyroid-type lattice structures included tunable parameters, which were useful to find out a convenient interconnected channeled structure having a porosity and mechanical properties close to those of the patient's bone. Both formulations can be described as follows:

Simple gyroid

$$f = \sin(x)\cos(y) + \sin(y)\cos(z) + \sin(z)\cos(x) - t \quad (9)$$

Double gyroid

$$f = [\sin(x)\cos(y) + \sin(y)\cos(z) + \sin(z)\cos(x)]^2 - t^2 \quad (10)$$

where  $x$ ,  $y$ , and  $z$  are the spatial coordinates,  $L$  is the unit length size of the cubic cell, and  $t$  is the volume surrounded by the gyroid-type surface. Unit length and porosity of both simple and double gyroid-type lattice structures were controlled by modifying the ratio spatial coordinates,  $L$  and  $t$ .

In order to evaluate the mechanical performance of the TPMS structures, two types of mechanical tests were performed experimentally on DMLS-printed samples. First, uniaxial compression tests were carried out, on  $10 \times 10 \times 10$  cell cubic arrays, at a loading rate of 1.8 mm/min, according to the ISO 13314 standard;<sup>37</sup> a universal MTS C45.105 testing machine with a maximum available applied load of 100 kN was employed. These tests were useful to reveal the strain–stress behavior of the lattice structures and allowed us to calculate the elastic modulus and maximum nominal compressive stress of each sample. The entire cross section of each sample was employed to estimate the corresponding nominal compressive stress value. It is important to point out that all measurements

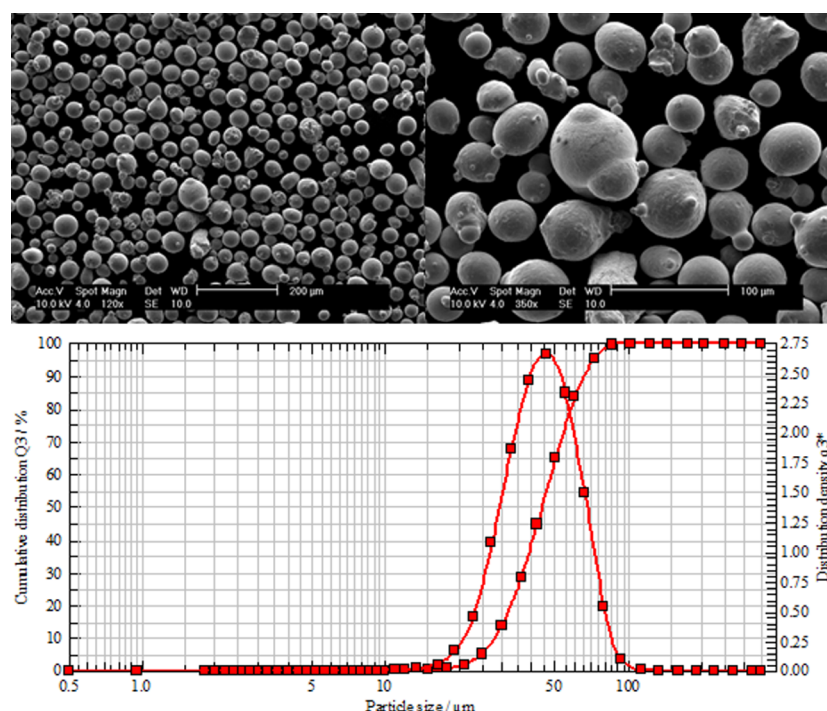


**Figure 11.** SEM micrographs and particle size distribution curve of the stainless-steel powder employed in the present study.

were performed using an AVX XT100 video extensometer to accurately measure sample deformation during testing. Each sample was black-colored in one face and 9 white equidistant points were painted on the same face to achieve a good contrast during measurements. At least three measurements of each type of lattice structure were performed in the present study. Additionally, the testing machine compliance was calculated in order to eliminate its contribution during the tests.

On the other hand, three-point bending tests were carried out at a loading rate of 3 mm/min, according to the ASTM D7250 standard,<sup>50</sup> the tests were performed in a calibrated 50 kN Instron 4482 universal machine. These tests were useful to reveal the flexural strength and to calculate the elastic modulus of each sample in this mode of load. It is important to remark that DMLS-printed samples used in the flexural tests were specially designed to comply with the requirements outlined in the aforementioned standard. In particular, the printed samples had a sandwich-like configuration containing the TPMS lattice structures at the center and two 200  $\mu\text{m}$ -thick solid walls at the top and bottom that acted as support surfaces for the test. Three samples for each type of lattice structure were tested to validate the results obtained.

**4.7. Additive Manufacturing of Lattice Structures and Customized Partial Hip Prosthesis.** TPMS lattice structures and a customized partial hip prosthesis were fabricated using a commercial DMLS system (EOS M280) equipped with a Yb-laser fiber (1040 nm) offering a maximum energy output of 400 W. The hip prosthesis was previously designed using CAD software (SolidWorks, USA) and converted into an STL file. The lattice structure was designed, as mentioned previously, using MATLAB software, and also converted into an STL file. Both STL files, from hip design and cellular structure, were processed employing Magics software (Materialise, US) to introduce the cellular structure within the hip prosthesis design. The file obtained was then analyzed in the

EOS RP-Tools 6.0 software (EOS, USA) in order to transform the data into a format suitable for the layer by layer construction process. The final file was then transferred to the EOS machine to start the manufacturing of the implant. The samples were printed using a commercially available stainless-steel powder (17-4 PH, EOS). This alloy powder has good corrosion resistance due to its high Cr content, being comparable with austenitic stainless steels. The morphology and particle size distribution of the stainless-steel powder was examined using scanning electron microscopy (SEM) (ESEM—Philips XL30) with a 15 kV accelerating voltage and secondary electrons (SE) radiation. A laser diffraction apparatus (HELOS/BR, Synpatec GmbH, Germany) was employed to obtain the particle size distribution of the stainless-steel powder. Figure 11 shows the typical spherical morphology of this type of powder and its particle size distribution. It presented a mean particle size ( $d_{50}$ ) of 44  $\mu\text{m}$  with a normal-type distribution.

3D printing of samples was performed in a controlled atmosphere chamber (filled with high purity nitrogen) to protect them against oxidation. The fabrication parameters were supplied by EOS GmbH for the stainless-steel powder employed in the present study.

Density of the printed porous lattice structures was verified experimentally and compared against theoretical values. Initially, the samples were decontaminated in a Branson 2510 ultrasonic cleaner using acetone in order to eliminate any residual material that could remain within the porous structure. This procedure was also employed to clean the final prosthesis prototype. Once cleaned, the samples were weighed in an analytical balance (Denver Instruments TP-214) and then infiltrated using paraffin. The weight of the infiltrated samples was measured, and the values obtained were then compared with those from the as-printed samples. Finally, the density of the lattice structures was calculated after the estimation of the air volume contained within the porous network and dividing

this value by the total volume of the structure. For the fabrication of the customized partial hip implant, a gyroid-type lattice structure was selected after verifying the experimental results obtained from the mechanical tests; the selected lattice structure was included in the implant CAD design. The CAD file was then converted into STL format and printed by DMLS employing a standard support structure.

## AUTHOR INFORMATION

### Corresponding Author

Carlos A. Poblano-Salas – CIATEQ A.C., Querétaro 76246, Mexico; [orcid.org/0000-0001-9375-6832](https://orcid.org/0000-0001-9375-6832);  
Email: [carlos.poblano@ciateq.mx](mailto:carlos.poblano@ciateq.mx)

### Authors

Jorge Corona-Castuera – CIATEQ A.C., Querétaro 76246, Mexico

Daniela Rodriguez-Delgado – CIATEQ A.C., Querétaro 76246, Mexico

John Henao – CONACyT-CIATEQ A.C., Querétaro 76246, Mexico

Juan Carlos Castro-Sandoval – CIATEQ A.C., Querétaro 76246, Mexico

Complete contact information is available at:

<https://pubs.acs.org/10.1021/acsomega.0c06144>

### Funding

This research was funded by the Mexican National Council of Science and Technology (CONACYT), specifically through projects CB 253365 and FOINS 297683.

### Notes

The authors declare no competing financial interest.

## ACKNOWLEDGMENTS

The authors would like to thank the funding provided to this work by the Mexican National Council of Science and Technology (CONACYT), especially through FOINS 297683 and CB 253365 projects. The authors are also grateful to CONACYT's Catedras program, project 848. CT-scan measurements were performed at PET/CT Unit, School of Medicine, UNAM, whereas mechanical testing of self-supported structures was carried out at CIDESI-CENTA; the support provided by both institutions is deeply appreciated. An IRB approval and a letter of consent were considered for the development of this research.

## REFERENCES

- (1) Pivec, R.; Johnson, A. J.; Mears, S. C.; Mont, M. A. Hip arthroplasty. *Lancet* **2012**, *380*, 1768–1777.
- (2) Katz, J. N. Preferences, Quality, and the (Under)utilization of Total Joint Arthroplasty. *Med. Care* **2001**, *39*, 203–205.
- (3) Kop, A. M.; Swarts, E. Selection of primary hip and knee arthroplasties for public hospitals in western Australia: a clinical evidence approach. *Aust. N. Z. J. Surg.* **2006**, *76*, 1068–1074.
- (4) Fischer, T.; Stern, C.; Fritz, B.; Zingg, P. O.; Pfirrmann, C. W. A.; Sutter, R. Impact of stem design and cementation on postoperative femoral antetorsion in 227 patients with total hip arthroplasty (THA). *Skeletal Radiol.* **2020**, *49*, 2001–2009.
- (5) Pedersen, A.; Johnsen, S.; Overgaard, S.; Søballe, K.; Sørensen, H.; Lucht, U. Registration in the Danish Hip Arthroplasty Registry: Completeness of total hip arthroplasties and positive predictive value of registered diagnosis and postoperative complications. *Acta Orthop. Scand.* **2004**, *75*, 434–441.

(6) Agaba, P.; Kildow, B. J.; Dhotar, H.; Seyler, T. M.; Bolognesi, M. Comparison of postoperative complications after total hip arthroplasty among patients receiving aspirin, enoxaparin, warfarin, and factor Xa inhibitors. *J. Orthop.* **2017**, *14*, 537–543.

(7) Lindberg-Larsen, M.; Petersen, P. B.; Jørgensen, C. C.; Overgaard, S.; Kehlet, H. Postoperative 30-day complications after cemented/hybrid versus cementless total hip arthroplasty in osteoarthritis patients > 70 years. *Acta Orthop* **2020**, *91*, 286–292.

(8) Gwam, C. U.; Mistry, J. B.; Mohamed, N. S.; Thomas, M.; Bigart, K. C.; Mont, M. A.; Delanois, R. E. Current Epidemiology of Revision Total Hip Arthroplasty in the United States: National Inpatient Sample 2009 to 2013. *J. Arthroplasty* **2017**, *32*, 2088–2092.

(9) Ngo, T. D.; Kashani, A.; Imbalzano, G.; Nguyen, K. T. Q.; Hui, D. Additive manufacturing (3D printing): A review of materials, methods, applications and challenges. *Composites, Part B* **2018**, *143*, 172–196.

(10) Baumers, M.; Dickens, P.; Tuck, C.; Hague, R. The cost of additive manufacturing: machine productivity, economies of scale and technology-push. *Technol. Forecast. Soc. Change* **2016**, *102*, 193–201.

(11) Tunchel, S.; Blay, A.; Kolerman, R.; Mijiritsky, E.; Shibli, J. A. 3D printing/additive manufacturing single titanium dental implants: a prospective multicenter study with 3 years of follow-up. *Int. J. Dent.* **2016**, *2016*, 8590971.

(12) Javadi, M.; Haleem, A. 3D printed tissue and organ using additive manufacturing: an overview. *Clin. Epidemiol. Glob. Health* **2020**, *8*, 586–594.

(13) Cronskär, M.; Bäckström, M.; Rännar, L. E. Production of customized hip stem prostheses - a comparison between conventional machining and electron beam melting (EBM). *Rapid Prototyp. J.* **2013**, *19*, 365–372.

(14) Baharuddin, M. Y.; Zulkifly, A. H.; Choo, L. A.; Aminudin, S. N. A.; Lee, M. H.; Salleh, S. H. S. Fabrication of Low-Cost Hip Implant using Direct Metal Laser Sintering Technique. *Int. J. Recent Technol. Eng.* **2019**, *8*, 4544–4547.

(15) Abdu, M. R.; Kamsah, N. Interface Micromotion of Cementless Hip Stems in Simulated Hip Arthroplasty. *Am. J. Appl. Sci.* **2009**, *6*, 1682–1689.

(16) Sundfeldt, M.; V Carlsson, L.; B Johansson, C.; Thomsen, P.; Gretzer, C. Aseptic loosening, not only a question of wear: A review of different theories. *Acta Orthop* **2006**, *77*, 177–197.

(17) Sadoghi, P.; Liebensteiner, M.; Agreiter, M.; Leithner, A.; Böhler, N.; Labek, G. Revision surgery after total joint arthroplasty: A complication-based analysis using worldwide arthroplasty registers. *J. Arthroplasty* **2013**, *28*, 1329–1332.

(18) Byrne, D. P.; Mulhall, K. J.; Baker, J. F. Anatomy & Biomechanics of the Hip. *Open Sports Med. J.* **2010**, *4*, 51–57.

(19) Piao, C.; Wu, D.; Luo, M.; Ma, H. Stress shielding effects of two prosthetic groups after total hip joint simulation replacement. *J. Orthop. Surg. Res.* **2014**, *9*, 71.

(20) Hazlehurst, K. B.; Wang, C. J.; Stanford, M. The potential application of a Cobalt Chrome Molybdenum femoral stem with functionally graded orthotropic structures manufactured using Laser Melting technologies. *Med. Hypotheses* **2013**, *81*, 1096–1099.

(21) Arabnejad, S.; Johnston, B.; Tanzer, M.; Pasini, D. Fully porous 3D printed titanium femoral stem to reduce stress-shielding following total hip arthroplasty. *J. Orthop. Res.* **2017**, *35*, 1774–1783.

(22) Limmahakhun, S.; Oloyede, A.; Sithiseripratip, K.; Xiao, Y.; Yan, C. Stiffness and strength tailoring of cobalt chromium graded cellular structures for stress-shielding reduction. *Mater. Des.* **2017**, *114*, 633–641.

(23) Hussein, A.; Hao, L.; Yan, C.; Everson, R.; Young, P. Advanced lattice support structures for metal additive manufacturing. *J. Mater. Process. Technol.* **2013**, *213*, 1019–1026.

(24) Yan, C.; Hao, L.; Hussein, A.; Young, P. Ti-6Al-4V triply periodic minimal surface structures for bone implants fabricated via selective laser melting. *J. Mech. Behav. Biomed. Mater.* **2015**, *51*, 61–73.

(25) Maietta, S.; Gloria, A.; Improta, G.; Richetta, M.; De Santis, R.; Martorelli, M. A Further Analysis on Ti6Al4V Lattice Structures



Manufactured by Selective Laser Melting. *J. Healthc. Eng.* **2019**, 2019, 3212594.

(26) Simoneau, C.; Brailovski, V.; Terriault, P. Design, manufacture and tensile properties of stochastic porous metallic structures. *Mech. Mater.* **2016**, 94, 26–37.

(27) Alkhatib, S. E.; Mehboob, H.; Tarlochan, F. Finite Element Analysis of Porous Titanium Alloy Hip Stem to Evaluate the Biomechanical Performance During Walking and Stair Climbing. *J. Bionic Eng.* **2019**, 16, 1103–1115.

(28) Rahmati, S.; Abbaszadeh, F.; Farahmand, F. An improved methodology for design of custom-made hip prostheses to be fabricated using additive manufacturing technologies. *Rapid Prototyp. J.* **2012**, 18, 389–400.

(29) Yáñez, A.; Herrera, A.; Martel, O.; Monopoli, D.; Afonso, H. Compressive behaviour of gyroid lattice structures for human cancellous bone implant applications. *Mater. Sci. Eng., C* **2016**, 68, 445–448.

(30) Abbaszadeh, F.; Rahmati, S.; Kheirollahi, H.; Farahmand, F. Design for manufacturing of custom-made femoral stem using CT data and rapid prototyping technology. *Int. J. Rapid Manuf.* **2011**, 2, 76.

(31) Mangano, C.; Bianchi, A.; Mangano, F. G.; Dana, J.; Colombo, M.; Solop, I.; Admakin, O. Custom-made 3D printed subperiosteal titanium implants for the prosthetic restoration of the atrophic posterior mandible of elderly patients: a case series. *3D Print. Med.* **2020**, 6, 1.

(32) ISO 7206-1. Implants for surgery—Partial and total hip joint prostheses Part-1: Classification and designation of dimensions, n.d.

(33) An, Y. H. Mechanical Properties of Bone. In *Mechanical Testing of Bone and the Bone-Implant Interface*, 1st ed.; An, Y. H., Draughn, R. A., Eds.; CRC Press: New York, 2000; pp 41–64.

(34) Hendrickson, N. R.; Pickhardt, P. J.; Del Rio, A. M.; Rosas, H. G.; Anderson, P. A. Bone Mineral Density T-Scores Derived from CT Attenuation Numbers (Hounsfield Units): Clinical Utility and Correlation with Dual-energy X-ray Absorptiometry. *Iowa Orthop. J.* **2018**, 38, 25–31.

(35) Muñoz Gutierrez, J. *Atlas de Mediciones Radiográficas en Ortopedia y Traumatología*, 2nd ed.; Mc Graw Hill: México, 2011; pp 93–117.

(36) Li, B.; Aspden, R. M. Composition and Mechanical Properties of Cancellous bone from the Femoral Head of Patients with Osteoporosis or Osteoarthritis. *J. Bone Miner. Res.* **1997**, 12, 641–651.

(37) ISO 13314. Mechanical testing of metals – Ductility testing – Compression test for porous and cellular metals, 2011. Int. Organ. Stand.

(38) Keller, T. S. Predicting the compressive mechanical behavior of bone. *J. Biomech.* **1994**, 27, 1159–1168.

(39) Ciarelli, T. E.; Fyhrie, D. P.; Schaffler, M. B.; Goldstein, S. A. Variations in Three-Dimensional Cancellous Bone Architecture of the Proximal Femur in Female Hip Fractures and in Controls. *J. Bone Miner. Res.* **2000**, 15, 32–40.

(40) Samper Gaitán, A.; Rojas Mora, F. A.; Narváez, D. M.; Mendez Moreno, L. M. Characterising structural, mechanical and cytotoxic properties of coral-based composite material intended for bone implant applications. *Ing. Invest.* **2011**, 31, 135–141.

(41) Mohamed, S.; Shamaz, B. H. Bone Tissue Engineering and Bony Scaffolds. *Int. J. Dent. Oral Heal.* **2015**, 1, 15–20.

(42) Liu, F.; Zhang, D.; Zhang, P.; Zhao, M.; Jafar, S. Mechanical Properties of Optimized Diamond Lattice Structure for Bone Scaffolds Fabricated via Selective Laser Melting. *Materials* **2018**, 11, 374.

(43) Schileo, E.; Dall'Ara, E.; Taddei, F.; Malandrino, A.; Schotkamp, T.; Baleani, M.; Viceconti, M. An accurate estimation of bone density improves the accuracy of subject-specific finite element models. *J. Biomech.* **2008**, 41, 2483–2491.

(44) Katz, Y.; Yosibash, Z. New insights on the proximal femur biomechanics using Digital Image Correlation. *J. Biomech.* **2020**, 101, 109599.

(45) Les, C. M.; Keyak, J. H.; Stover, S. M.; Taylor, K. T.; Kaneps, A. J. Estimation of material properties in the equine metacarpus with use of quantitative computed tomography. *J. Orthop. Res.* **1994**, 12, 822–833.

(46) Engelke, K.; Libanati, C.; Fuerst, T.; Zysset, P.; Genant, H. K. Advanced CT based In Vivo Methods for the Assessment of Bone Density, Structure, and Strength. *Curr. Osteoporos. Rep.* **2013**, 11, 246–255.

(47) Giambini, H.; Dragomir-Daescu, D.; Huddleston, P. M.; Camp, J. J.; An, K.-N.; Nassr, A. The Effect of Quantitative Computed Tomography Acquisition Protocols on Bone Mineral Density Estimation. *J. Biomech. Eng.* **2015**, 137, 114502.

(48) Synek, A.; Chevalier, Y.; Baumbach, S. F.; Pahr, D. H. The influence of bone density and anisotropy in finite element models of distal radius fracture osteosynthesis: Evaluations and comparison to experiments. *J. Biomech.* **2015**, 48, 4116–4123.

(49) Schileo, E.; Pitocchi, J.; Falcinelli, C.; Taddei, F. Cortical bone mapping improves finite element strain prediction accuracy at the proximal femur. *Bone* **2020**, 136, 115348.

(50) D7250/D7250M-16, A., 2016. Standard Practice for Determining Sandwich Beam Flexural and Shear Stiffness. ASTM Int.